Suess, E., von Huene, R., et al., 1990
Proceedings of the Ocean Drilling Program, Scientific Results, Vol. 112

45. MODELING OF PORE PRESSURE, CENTRAL PERU MARGIN[1]

Yaolin Shi,[2,3] Chi-Yuen Wang,[2] and Roland von Huene[4]

ABSTRACT

Based on available geological data and Ocean Drilling Program (ODP) Leg 112 drilling results, we made a preliminary model of pore pressures at the Peru margin at about 9°S. The predicted pore-pressure parameter τ^* (the ratio of the excess pore pressure and the difference between the lithostatic and hydrostatic pressures) is 0.5 or less beneath the lower slope and decreases to zero beneath the middle and upper slopes, which is much lower than that estimated for the Barbados accretionary prism (Shi and Wang, 1988).

SCIENTIFIC OBJECTIVES

Drilling along convergent margins during the Deep Sea Drilling Project was commonly thwarted by poor hole conditions, which caused many holes to be abandoned above the depth of the primary objectives. Unstable hole conditions were experienced at sites positioned where seismic-reflection records indicated little tectonic deformation, as well as others where there was considerable tectonism. The indications of elevated pore pressure at sites on the Japan Trench convergent margin, including two sites landward of the trench slope (Arthur et al., 1980), and on the Barbados (Watkins, Moore, et al., 1982) and Guatemalan (von Huene, 1985) margins, suggested an association between difficult drilling and overpressured pore fluids. Thus, before the drilling during Leg 112, we obtained support from the U.S. Science Advisory Committee of JOI (USSAC) to model the pressure field of the Peru margin to avoid, in so far as possible, high pore-fluid pressures during the leg. By avoiding areas of high pore pressure, we hoped to alleviate not only the problem of failed holes above targeted horizons, but also areas that might warrant caution for safety considerations. This paper is a preliminary study based upon pre-drilling data; the results of this study are compared with some post-drilling observations.

GEOLOGICAL SETTING

During planning for Leg 112, three transects along the Peru convergent margin were targeted for drilling to tectonic objectives. We modeled the central transect near 9°S to obtain an estimate of pore-fluid pressure. At 9°S, the bulk of the margin consists of a landward part with continental affinity against which a 15-km-wide prism of trench and oceanic material has been accreted (Fig. 1). A continental affinity is observed across the shelf, underlain by two forearc basins filled with stratified sediment that are separated by a low basement ridge. The upper slope also has a lens-shaped stratified sequence up to 1.5 km thick. Samples from the basement underlying the stratified sequences are of continental crystalline metamorphic and intrusive rocks of Paleozoic to Mesozoic age (Kulm et al., 1985). This acoustic basement with sediment of variable thickness ends at the middle slope coincident with a topographic break. The boundary with the adjacent accretionary lower slope is not imaged well enough to see the shape of the buttress. Lower-slope accreted sediment is recognized by numerous packets of landward-dipping reflections (Fig. 1).

At 9°S, the bathymetry is also separated by a mid-slope terrace into two regimes of different character (Fig. 2). This terrace separates a smooth upper slope from a rougher lower slope, which is consistent with the interpretation of the smooth upper slope as the floor of the forearc basin and rougher lower slope as accreted sediments in the seismic-reflection data (Bourgois et al., 1988). What becomes obvious in the bathymetry of the lower slope and trench is the impending collision of a ridge about 2 km above the floor of the trench at a point where the principal seismic record traverses the trench axis. Sediment ponded in the trench axis thins where the base of the ridge impinges against the lower slope. Thus, estimates of the volume of sediment in the trench axis at 9°S, using the principal multichannel record (Miller et al., 1986), were 500 m less than thicknesses observed in subsequent seismic data, also at 9°S (Bourgois et al., 1988).

Reprocessing of the multichannel seismic record imaged truncated reflections interpreted as strata cut by thrust faults within the accretionary complex (von Huene et al., 1985). Major thrust faults were interpreted to merge in a décollement (>15 m thick) above a subducting sediment sequence (Fig. 1). Much of the subducting sediment beneath the lower slope appears in pockets interpreted as graben in the oceanic crust. Subducting sediment nearly 1 km thick is observed beneath the middle slope and the foot of the upper slope, beyond which its image has been obscured by the first "water-bottom" multiple. The upper slope is dominated by normal faults that displace the slope sediment sequences (Fig. 1). The obscured structure of the mid-slope area could not be clarified sufficiently (despite much effort during reprocessing of the seismic data) to show the structural juncture between the crust of continental affinity and the accretion complex.

To construct the depth section (Fig. 1), seismic-refraction velocities were used. The refraction observations were made by shooting 60- to 70-km-long lines (Jones, 1981). This produced an average velocity over tens of kilometers that, when applied to the reflection data, probably smeared out any abrupt changes in velocity structure of the middle slope. However, the general configuration and structure of the crustal section (Fig. 1) is of sufficient precision for our modeling.

[1] Suess, E., von Huene, R., et al., 1990. *Proc. ODP, Sci. Results*, 112: College Station, TX (Ocean Drilling Program).
[2] Dept. of Geology and Geophysics, University of California, Berkeley, CA 94720.
[3] Dept. of Earth Sciences, Graduate School, Academia Sinica, P.O. Box 3908, Beijing, People's Republic of China.
[4] U.S. Geological Survey, Menlo Park, CA 94025.

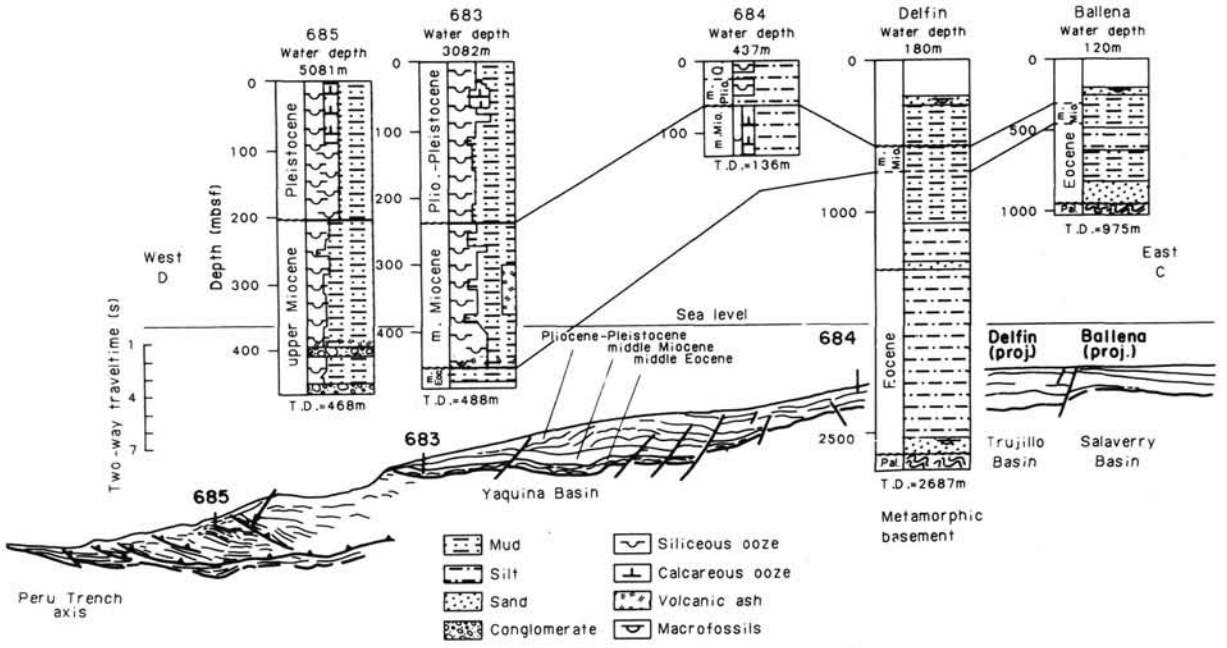

Figure 1. Interpreted time section of seismic record along line C-D in Figure 2, and columnar sections of Leg 112 drilling site along this line (from von Huene, Suess, et al., 1988).

Studies of Leg 112 cores provided physical properties (Marsters and Hill, this volume) and also ages and environments of deposition of the sediment sequences (Suess, von Huene, et al., 1988). Eocene sediment was deposited in shelf and upper-slope water depths that are considerably shallower than the depths from which the samples were recovered. The difference in water depth requires regional subsidence of the margin, which is thought to have occurred during subcrustal erosion beneath the trench slope and was accentuated during subduction of the Nazca Ridge (Suess, von Huene, et al., 1988). About 5 Ma, accretion along the lower slope began, and it appears to have continued unbroken since that time. The Eocene and greater age of upper and middle slope rocks and the young offscraped sediment of the lower slope may explain the precipitous decrease in heat flow seaward of the middle slope (Yamano and Uyeda, this volume).

The cores from Leg 112 locally displayed numerous dewatering pathways. Migration pathways were particularly easy to observe because of the well-preserved sediment structure in the oxygen-minimum zone, where bioturbation had not destroyed the fine lamination and bedding. Many of the observed vein structures and clay-filled fractures (Lindsley-Griffin et al., and Kemp and Lindsley-Griffin, this volume) were from sites on or near the continental shelf. Some of the strongest evidence for fluid migration was from the chemistry of interstitial waters (see Kastner et al., this volume). Water may have originated in the subducting sediments and may have migrated upward through 4 to 8 km of the upper plate.

PRINCIPLES OF COUPLED MODELING

The basic equations and nonlinear material properties controlling the dynamic, hydraulic, and thermal processes in sediments were discussed in detail elsewhere (Shi and Wang, 1986, 1988). The basic differential equation for porous flow under the effects of external loading, aquathermal pressuring, and other source terms is

$$(\alpha_b + n\beta)\frac{DP}{Dt} = \frac{1}{\rho_w}\nabla \cdot \left(\frac{\rho_w k}{\eta}\nabla(P - \rho_w \phi)\right) + \alpha_b \frac{DP_t}{DP} + n\lambda_w \frac{DT}{Dt} + h\,, \quad (1)$$

where P is pore pressure, ρ_w is the density of water, α_b is the drained bulk compressibility, n is the porosity, β is the compressibility of water, γ_w is the thermal expansion coefficient of water, P_t is the total mean stress due to overloading and tectonic compression, ϕ is the gravitational potential, T is temperature, k is the absolute permeability, η is the viscosity of water, and h is the source or sink of water due to dehydration of clays and other causes. $D(\ )/Dt$ is the material differential in the deforming coordinates. In fixed coordinates, $D(\ )/Dt = \delta(\ )/\delta t + \vec{U},5 \cdot \nabla(\ )$, where $\vec{U}$, is the velocity of sediment matrix with respect to the fixed coordinates.

The rate of change of pore pressure is affected by the following source terms.

1. The rate of change in the total pressure, P_t, which is a result of mechanical pressuring from changes in overburden and/or tectonic compression. This is the most important term in pore-pressure generation.
2. The rate of change in temperature, which contributes to the "aquathermal" pressuring. This term turns out to be insignificant in ordinary geological circumstances (Shi and Wang, 1986).
3. Other source terms, such as mineral dehydration, changes of porosity caused by creep of the solid skeleton of sediments, or chemical processes, are not included because of a lack of well-known experimental information.

In subduction environment, the mechanical pressuring source term in Equation 1 can be expressed in terms of the subduction velocity, $\vec{U}$, and the dip angle of the descending plate, β,

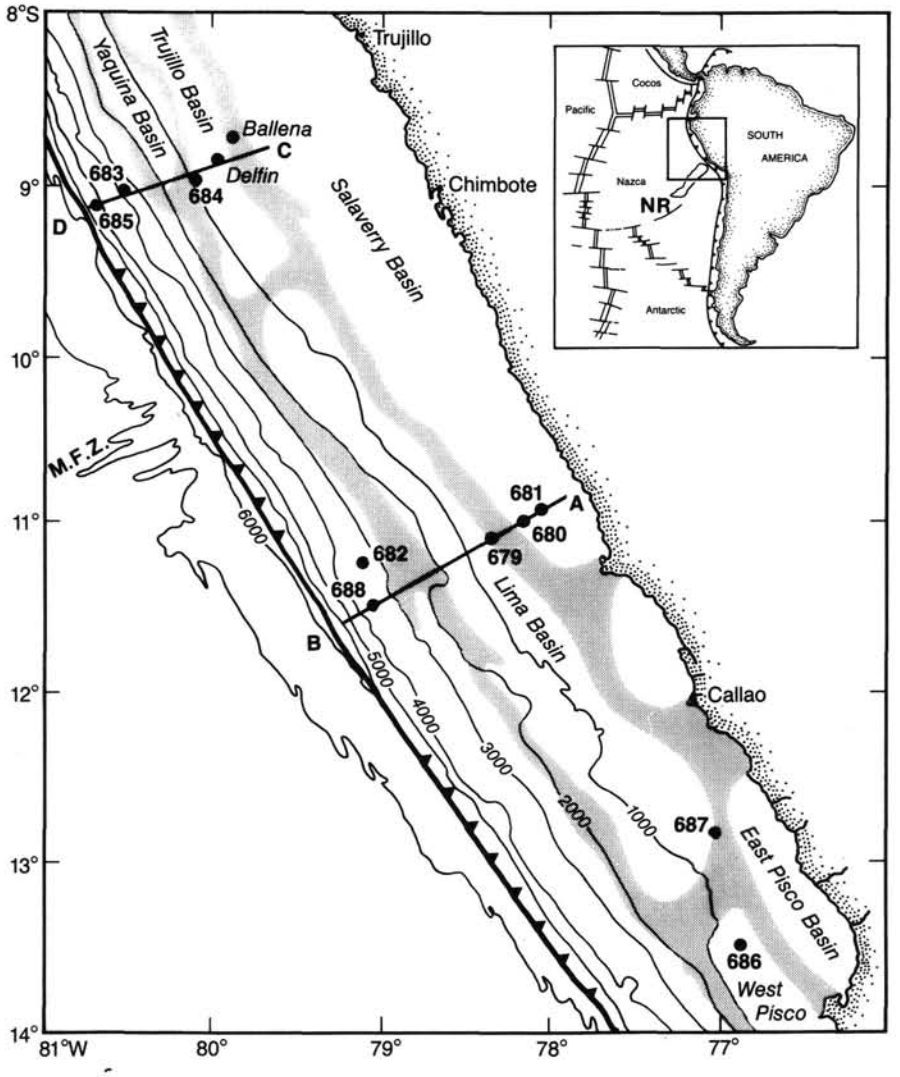

Figure 2. Peru continental margin bathymetry, showing locations of drill sites of Leg 112 and seismic-reflection lines. Line with barbs indicates Peru Trench convergence zone. NR = Nazca Ridge, MFZ = Mendaña Fracture Zone (from von Huene, Suess, et al., 1988).

$$\frac{DP_t}{D_t} = \frac{\delta P_t}{\delta t} + U\cos\beta\frac{\delta P_t}{\delta x} + U\sin\beta\frac{\delta P_t}{\delta y}. \qquad (2)$$

Overloading because of sedimentation or dewatering of overlying sediments will cause local change of total stress with time; total stress gradient is determined by gravitational and tectonic forces. Both factors can cause pore pressure to increase when sediments are subducted at velocity, $\vec{U}$.

The equation for heat transfer is

$$C\rho\frac{DT}{Dt} + c_w P_w \vec{q} \cdot \nabla(T) = \nabla \cdot (K\nabla T) + Q, \qquad (3)$$

where c is the bulk specific heat, K is the bulk thermal conductivity, ρ is the bulk density, $\vec{q}$ is the discharge of water, c_w is the specific heat of water, and Q is the heat source in unit volume. The first term in the right-hand side is the conductive term, and the second one is the heat source. There are two kinds of advective heat transfer: (1) an advective transfer due to matrix motion, which is implicitly included in the DT/Dt term on the left-hand side of the equation, and (2) an advective transfer due to porous fluid flow with respect to the matrix, which is explicitly expressed in the second term on the left-hand side of the equation.

The change in volume or density of sediments is primarily related to porosity that decreases under increasing effective pressure. An empirical relationship was given by Athy (1930),

$$n = n_0 \exp(bP_e), \qquad (4)$$

where n_0 is the porosity at surface and b is a material parameter. The value of b can be calculated from the observed data of porosity vs. depth or from laboratory experiments. For clays and silts from Middle America Trench (DSDP Leg 84), n_0 ranges from 0.7 to 0.8, and the value of b is about 1.1×10^{-8} Pa^{-1}.

Permeability of different clays as functions of effective stress up to 200 MPa (Morrow et al., 1984) can be fit fairly closely with an empirical relationship (Shi and Wang, 1986):

$$k = k_0\left(\frac{P_e}{P_0}\right)^{-f}, \qquad (5)$$

where k_0 and f are experimentally determined constants. P_0 is the pressure at the surface and k_0 can be interpreted as the permeability at the surface; k_0 ranges from 10^{-18} to 10^{-14} m^2 (1 μd to 10 md) for clays, and f ranges from 1.2 to 1.8 for loading and from 0.4 to 0.9 for unloading. For clays and silts from the Middle America Trench, k_0 ranges from 10^{-16} to 10^{-12} m^2 (0.1 md to 1d), and f is about 1.55. Here, we assume these values as similar data are lacking for the Peru margin.

The viscosity of water depends mainly on temperature as (Mercer et al., 1975),

$$\frac{1}{\eta} = 5380 + 5800A - 260A^3 , \tag{6}$$

where $A = (T - 150)/100$, T is in °C, η is in Pa · s.

The compressibility of water β is about 4×10^{-10} Pa^{-1}. The bulk compressibility of sediments, α_b, is affected by both the changes in pore space and the compression of the solid grains as

$$\alpha_b = \frac{\alpha_n}{(1 - n)} + n\alpha_s . \tag{7}$$

The compressibility of solid grain, α_s, is small (of the order of 10^{-11} Pa^{-1}). The porosity compressibility, α_n ranges from 10^{-9} to 10^{-8} Pa^{-1}, which can be calculated from the available empirical relationships between effective stress and porosity. For Athy's relationship (Eq. 4) we have $\alpha_n = nb$.

The specific heat of a saturated porous medium can be calculated from (Smith, 1973)

$$c = c_w n + c_s(1 - n) , \tag{8}$$

where c_w is the specific heat of the fluid component and c_s is the specific heat of the solid component. Similar relationships hold for density, heat source, and other extensive variables. The bulk thermal conductivity of the sediment, K, can be calculated from that of its components of water, K_w and solid grains, K_s, by using the following relationship from Lewis and Rose (1970):

$$K = K_s\left(\frac{K_w}{K_s}\right)^n . \tag{9}$$

A finite-element method (FEM) is used in this study. This method has the advantage that a fine grid can be used for the region of interest to increase the resolution, while a coarse grid can be used outside of this region to reduce the cost of computation. A two-dimensional model was used to attain a quasi-steady state solution for the overall pattern.

The finite-element formulation of the diffusion equations for both porous flow and heat transfer can be obtained by using a standard Galerkin method (e.g., Zienkiewicz, 1977). The relative importance of the advective transfer in comparison with the diffusive transfer is determined by the magnitude of the Peclet number, P_{ec}. Spurious oscillations occur in the finite-element computation using the ordinary Galerkin formulation when the Peclet number becomes greater than one. Thus, a streamline upwind scheme by Hughes and Brooks (1980) is used. For advection-dominated problems, this method gives stable and accurate solutions.

The coupled nonlinear equations for porous flow and for heat transfer are solved through the following procedure: For given initial conditions of pore pressure and temperature with proper boundary conditions, the pressure- and temperature-dependent material properties can be determined. Pore pressure and temperature are then calculated after the first time step. Hydraulic and thermal properties of sediments are updated according to the newly computed pore pressure and temperature. In the two-dimensional problem, we use a fixed grid, while in the one-dimensional modeling, we use a deformable grid; thus, the advective term due to matrix motion does not appear explicitly, but nodal coordinates have to be updated at every time step. This procedure is repeated for the next time step, and the evolution of pore pressure and temperature in the subduction complex then can be computed. A backward difference scheme is chosen to enhance numerical stability.

When choosing the intervals of time steps, there is a trade-off between accuracy and computer time. Because of the high nonlinearity in porosity and permeability as functions of effective stress, oscillation may occur in problems in which pore pressure approaches lithostatic pressure, if the time step is not small enough.

Two end-members are chosen for modeling the pore pressure of the Peru complex. One has a thin layer of sediments on the oceanic plate (150 m) and a thin trench fill (320 m), which corresponds to earlier interpretation of multichannel record (Miller et al., 1986). The other has a thicker layer of sediments on the oceanic plate (180 m) and a thick trench fill (750 m), which corresponds to revised interpretation of sediment thickness based on subsequent seismic data (Bourgois et al., 1988; Moore and Taylor, 1988). The former will be denoted as Model N, and the latter as Model K.

In both models, the lower layer consists of pelagic sediments (Yeats et al., 1976) with low permeability ($k_0 = 10^{-16}$ m^2 = 0.1 md). The upper prism is supposed to be semipelagic sediments with high permeability (k_0 = 1 md) (Kulm et al., 1985).

The following boundary conditions are assumed in the computation. For the problem of porous flow, the excess pore pressure on the upper surface of the model is zero; the base of the prism is assumed to be impermeable. The vertical boundaries are located at 35 km landward and 5 km oceanward of the trench, respectively; the horizontal components of porous flow across both vertical boundaries are most likely to be small and are assumed to be negligible. For the thermal problem, temperature at the upper surface should be 0°C. At the two vertical side boundaries, horizontal component of heat flow should be zero. The lower boundary is taken at a depth of 70 km, instead of at the base of sediments. A constant temperature of 1400°C is assumed at this boundary.

As Equations 1 and 3 indicate, the kinematics of sediments are critical for computing the evolution of pore pressure and temperature in subduction complexes. In this model, the pelagic sediments above the oceanic plate are carried down beneath the prism, with the subducting plate at a velocity of about 10 cm/yr, consistent with seismic and plate-tectonic observations.

The initial temperatures are calculated from a cooling, spreading plate model. The initial pore pressures are inferred to be hydrostatic. Once the initial conditions of pore pressure and temperature are given, iterations over many time steps are used to calculate pore pressure and temperature, until a steady state solution for pore pressure has been reached. We have conducted numerical experiments and found that the results of computation converge to the same solution for reasonable initial pore pressures.

MODELING RESULTS

The results of our modeling are presented in terms of several parameters that are defined below:

1. The excess pore pressure, P'. This is defined as the difference between the computed pore pressure, P, and the hydrostatic pressure, P_{hydr},

$$P' = P - P_{hydr} . \quad (10)$$

In a diagram showing the spatial distribution of P', the normal of the contours gives the direction of porous flow. The excess pore pressure increases with depth, but remains significantly below the lithostatic pressure (Figs. 3 and 4).

2. The Hubbert-Rubey pore-pressure parameter, λ. This is defined as the ratio between pore pressure, P, and the lithostatic pressure, P_{lith} (Hubbert and Rubey, 1959):

$$\lambda = \frac{P}{P_{lith}} . \quad (11)$$

This was further modified by Davis et al. (1983) to include the weight of the overlying water column for sediments under water:

$$\lambda = \frac{P - P_w g D}{P_{lith} - P_w g D} , \quad (12)$$

where D is the thickness of the water column.

λ changes from zero when pore pressure is zero to 1, as pore pressure equals the lithostatic value. However, λ may not be an ideal parameter for demonstrating the relative magnitude of pore pressure in sediments with changing porosity; the value of λ is not a constant for hydrostatic pore pressure. For example, when the porosity of the overlying sediments is 0.7 or higher, λ at the hydrostatic pressure is 0.66; but when the porosity approaches zero, λ at the hydrostatic pressure is 0.37. Hence, the interpretation of λ varies with the distribution of porosity.

3. The excess pore-pressure parameter, λ^*. This is defined as the ratio of the excess pore pressure and the differential pressure between the lithostatic and hydrostatic pressures,

$$\lambda = \frac{P - P_{hydr}}{P_{lith} - P_{hydr}} = \frac{P'}{P_{lith} - P_{hydr}} , \quad (13)$$

where λ^* is zero when pore pressure is hydrostatic and approaches 1 when pore pressure approaches lithostatic load. For problems where large changes in porosity occur, λ^* may be a better parameter than λ for showing the presence and the relative magnitude of the excess pore pressure.

4. Effective stress, P_e. This is defined as P_t, − P, where P_t, $= \rho g h$, h is the thickness of overburden, and $\rho = n\rho_w + (1 - n)\rho_s$.

Various models have been computed and compared. The input parameters used in two of the models are given in Table 1.

Model N

This model has a thin trench fill; it has a small plate dip beneath the trench (2°), but a greater plate dip beneath the lower slope (13°). The results are shown in Figure 3. Excess pore pressures are generated when the pelagic layer is carried down by the subducting oceanic plate. The excess pore-pressure parameter, λ^* (Fig. 3C) is low in the trench ($\lambda^* = 0.3$), but increases beneath the lower slope, reaching a maximum value of 0.75 at a depth of about 3.5 km. Farther landward, λ^* decreases, the effective stress increases, and porosity decreases both landward and downward. However, near the subducting pelagic layer, pore pressure is higher and the effective stress and porosity exhibit a reversed trend.

Model K

This model has a thick trench fill. The plate dip beneath both the trench and the lower slope has been changed to 9° to accommodate the thicker sediments. This angle is greater than that of Model N at the trench, but smaller beneath the lower slope. The results are shown in Figure 4. Pore pressure is generated when the sedimentary layer is carried down by the subducting oceanic plate. The excess pore-pressure parameter, λ^* (Fig. 4C) becomes moderately high in the trench ($\lambda^* = 0.6$), but increases only slightly beneath the lower slope; farther landward, λ decreases, the effective stress increases, and porosity decreases in similar patterns as in Model N.

The differences in pore pressures in the two models can be interpreted in the following way: As sediments are subducted under the prism, the increased overburden compacts the sediments and generates excess pore pressures. In the trench of Model K, the plate dip is greater and the overlying layer is thicker than those in Model N. Thus, the predicted excess pore pressures tend to be higher. Under the lower slope, the plate dip is smaller in Model K than that in Model N; thus, pore pressures are lower in Model K than those in Model N in this part of the prism.

In both models, excess pore pressures decrease landward beneath the middle and upper slope and the outer continental shelf. This is partly due to the flattening of the plate dip (about 1°), which leads to a decrease in loading rate, and partly due to the decreased compressibility of the dewatered and compacted sediments. Dehydration of clays and diatomites at increasing P and T, which may produce higher pore pressures than those computed, is not included here.

In both models, the predicted pore pressures at the drilling sites are low. The predicted pore pressure is sublithostatic at Site 685, with $\lambda^* = 0.5$ at a depth of 1 km for Model N, and $\lambda^* = 0.3$ at the same depth for Model K. At all other drilling sites, the predicted λ^* values are lower than these values.

CONCLUSIONS

This paper presents a preliminary model of the Peru margin based on pre-drilling data. Modeling results predict that pore pressures at all drilling sites are moderately low. Because no high pore pressures were encountered during Leg 112 drilling, we consider the modeling results consistent with observations.

The low pore pressure (nearly hydrostatic) and high effective pressure at this margin may imply relatively high shear stresses at the dècollement. If so, frictional heating may be an important heat source affecting the thermal structure of this margin. Finally, this is a first model, and further refinement is possible now that, as reported in this volume, the tectonic history and physical properties are known more precisely.

ACKNOWLEDGMENTS

This study was supported by the National Science Foundation and the Joint Oceanographic Institutions, Inc. The comments from two anonymous reviewers have helped greatly in improving the paper. Any opinions, findings, and conclusions or recommendations expressed here are those of the authors and do not necessarily reflect the views of the National Science Foundation, the Joint Oceanographic Institutions, Inc., or Texas A&M University. Computer time was subsidized by the Computer Center of the Berkeley Campus.

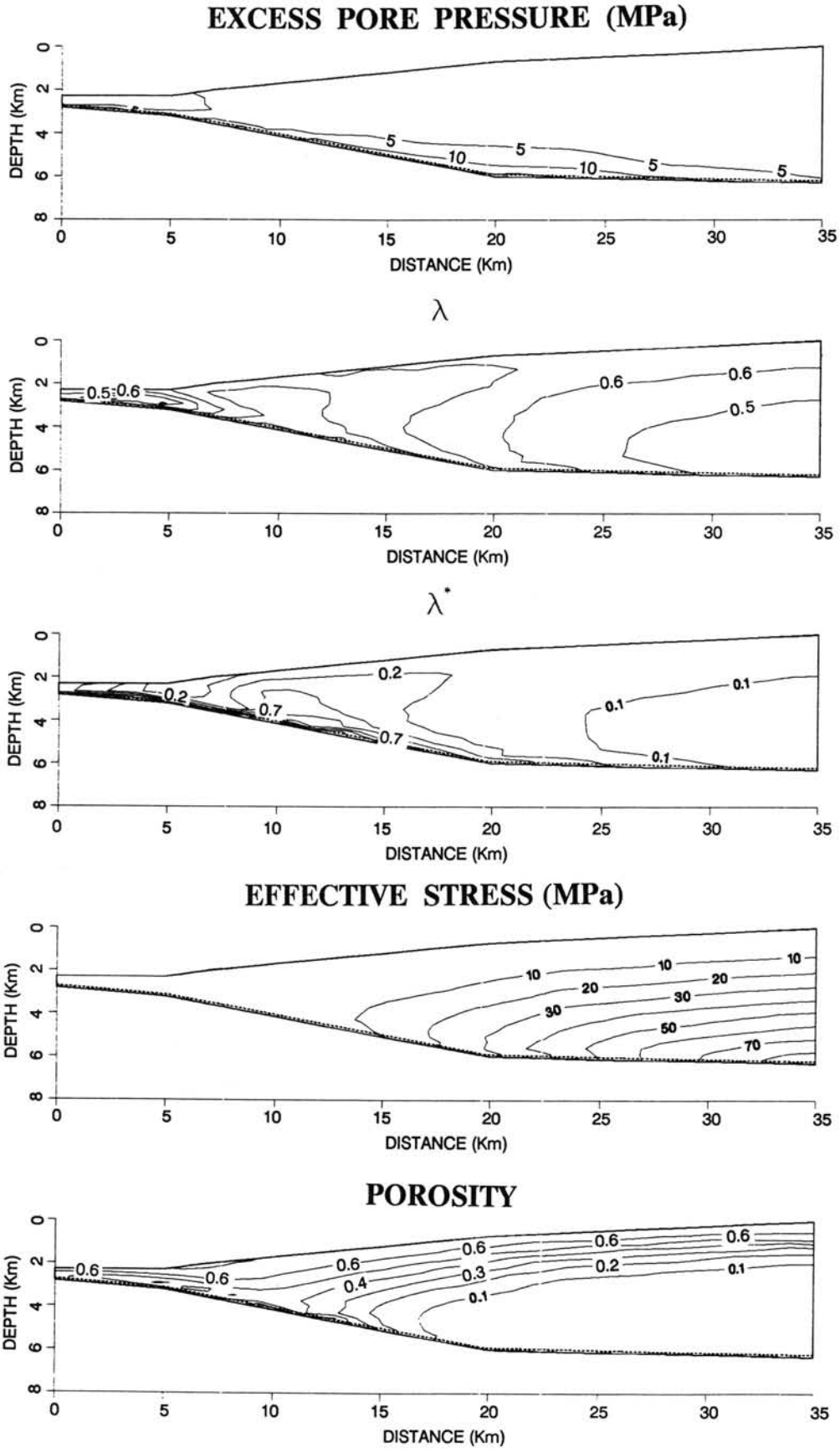

Figure 3. Modeling results for Model N, with thin trench fill.

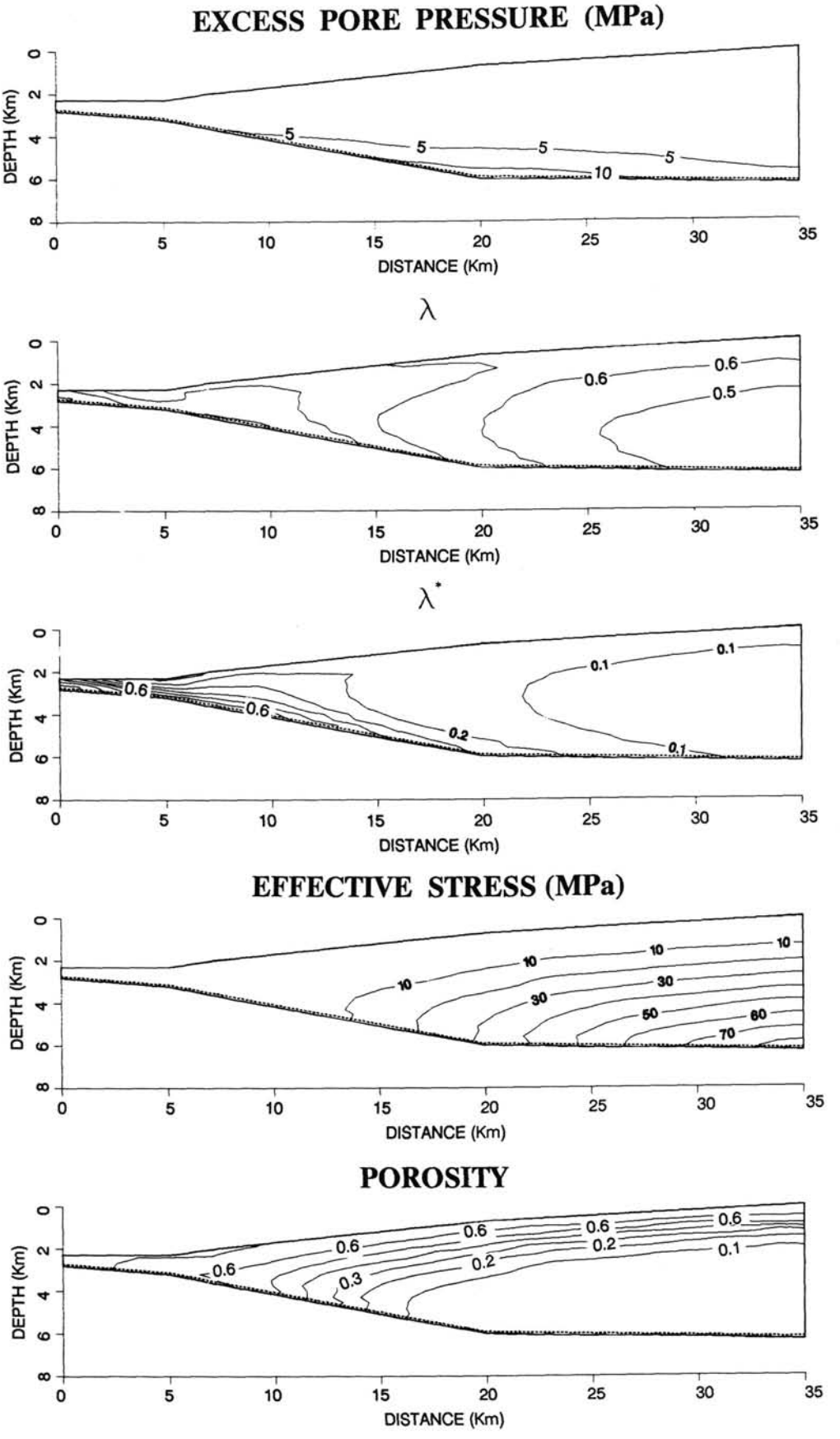

Figure 4. Modeling results for Model K, with thick trench fill.

Table 1. Parameters for sediment properties used in modeling.

Permeability	Pelagic sediments	Semipelagic sediments
k_0 (m^2)	1.0×10^{-16}	1.0×10^{-15}
p virgin	1.55	1.55
swelling	0.70	0.70
Porosity		
n_0	0.6	0.75
b (Pa^{-1}) virgin	1.1×10^{-7}	1.1×10^{-7}
b' (Pa^{-1}) swelling	1.0×10^{-8}	1.0×10^{-8}
Thermal conductivity (cal cm^{-1} s^{-1} $°C^{-1}$)		
K_s	0.006	0.006
K_w,	0.0014	0.0014
K_m (mantle)	0.007	0.007
Specific heat (cal g^{-1} $°C^{-1}$)		
c_w	1.0	1.0
c_s	0.2	0.2
c_m (mantle)	0.2	0.2
Compressibility (Pa^{-1})	4.0×10^{-10}	
Thermal expansion ($°C^{-1}$)	4.0×10^{-4}	
Density (kg m^{-3})		
ρ_w	1000	
ρ_s	2700	
ρ_m (mantle)	3300	
Temperature (°C)		
surface	0	
at 70 km	1400	

REFERENCES

Arthur, M. A., Carson, B., and von Huene, R., 1980. Initial tectonic deformation of hemipelagic sediment at the leading edge of Japan convergent margin. *In* Lee, M., Stout, L., et al. (Eds.), *Init. Repts. DSDP*, 56, 57: Washington (U.S. Govt. Printing Office), 568–615.

Athy, L. F., 1930. Density, porosity and compaction of sedimentary rocks, *AAPG Bull.*, 14:1–35.

Bourgois, J., Pautot, G., and Bandy, W., 1988. Seabeam and seismic-reflection imaging of the tectonic regime of the Andean continental margin off Peru (4°S to 10°S). *Earth Planet. Sci. Lett.*, 87:111–126.

Davis, D., Suppe, J., and Dahlen, F. A., 1983. Mechanics of fold-and-thrust belts and accretionary wedges. *J. Geophys. Res.*, 88:1153–1172.

Hubbert, M. K., and Rubey, W. W., 1959. Role of fluid pressure in mechanics of overthrust faulting. 1, Mechanics of fluid-filled porous solids and its application to overthrust faulting. *Geol. Soc. Am. Bull.*, 70:115–166.

Hughes, T.J.R., and Brooks, A., 1980. A multi-dimensional upwind scheme with no crosswind diffusion. *In* Hughes, T.J.R. (Ed.), *Finite Element Methods for Convection Dominated Flows:* New York (Am. Soc. Mech. Engrs.), 19.

Jones, P. R., III, 1981. Crustal structures of the Peru continental margin and adjacent Nazca plate, 9°S latitude. *Geol. Soc. Am. Mem*, 154:423–443.

Leg 112 Shipboard Scientific Party, 1987. Leg 112: Studies of continental margin. *Geotimes*, 32:10–12.

Mercer, J. W., Pinder, G. F., and Donaldson, I. G., 1975. A Galerkin finite element analysis of the hydrothermal system at Irakei, New Zealand. *J. Geophys. Res.*, 80:2608–2621.

Miller, J., Hussong, D., and von Huene, R., 1986. Peru continental margin, record section 3. *In* von Huene, R. (Ed.), *Seismic Images of Modern Convergent Margin Tectonic Structure*. AAPG Studies in Geology, 26:32–33.

Morrow, C. A., Shi, L., and Byerlee, J. D., 1984. Permeability of fault gouge under confining pressure and shear stress. *J. Geophys. Res.*, 89:3193–3200.

Shi, Y. and Wang, C.-Y., 1986. Pore pressure generation in sedimentary basins: overloading versus aquathermal. *J. Geophys. Res.*, 91:2153–2162.

_____, 1988. Generation of high pore pressures in accretionary prisms: inferences from the Barbados subduction complex. *J. Geophys. Res.*, 93:8893–8910.

Smith, J. E., 1973. Shale compaction. *J. Soc. Pet. Engrs.*, 13:12–22.

Suess, E., von Huene, R., et al., 1988. *Proc. ODP, Init. Repts.*, 112: College Station, TX (Ocean Drilling Program).

von Huene, R., 1985. Direct measurement of pore fluid pressure, Log 84, Guatemala and Costa Rica. *In* von Huene, R., Aubouin, J., et al. (Eds.), *Init. Rept. DSDP*, 84: Washington (U.S. Govt. Printing Office), 767–772.

von Huene, R., and Lee, H., 1983. The possible significance of pore fluid pressures in subduction zones. *AAPG Mem.*, 781–791.

von Huene, R., Kulm, L. D., and Miller, J., 1985. Structure of the frontal part of the Andean convergent margin. *J. Geophys. Res.*, 90:5429–5442.

von Huene, R., Suess E., and Leg 112 Shipboard Scientists, 1988. Ocean Drilling Program Leg 112, Peru continental margin: Part 1, tectonic history. *Geology*, 16:934–938.

Wang, C.-Y., Shi, Y., and von Huene, R., 1987. Thermal structure of two convergent margins—Subduction accretion vs. subduction erosion. *Eos, Trans. Am. Geophys. Union*, 68:1469.

Watkins, J. S., Moore, J. C., et al., 1982. *Init. Repts. DSDP*, 66: Washington (U.S. Govt. Printing Office).

Yeats, R. S., Hart, S. R., et al., 1976. *Init. Repts. DSDP*, 34: Washington (U.S. Govt. Printing Office), 803–814.

Zienkiewicz, O. C., 1977. *The Finite Element Method*, 3rd ed.: New York (McGraw-Hill).

Date of initial receipt: 13 December 1988
Date of acceptance: 3 August 1989
Ms 112B-201